physica status solidi

Theoretical vibrational optical activity of chiral carbon nanoparticles: fullerenes and carbon nanotubes

Péter R. Nagy[*,1], **László Biró**[*,2], **János Koltai**[2], **Péter R. Surján**[1], **Ágnes Szabados**[1], **Jenő Kürti**[2]

[1] Laboratory of Theoretical Chemistry, Eötvös University (ELTE), Pázmány P. sétány 1/A, 1117 Budapest, Hungary
[2] Department of Biological Physics, Eötvös University (ELTE), Pázmány P. sétány 1/A, 1117 Budapest, Hungary

Received XXXX, revised XXXX, accepted XXXX
Published online XXXX

Key words: Raman optical activity, chiral carbon nanotubes and fullerenes, tight-binding approximation, density functional theory

[*] Corresponding author: e-mail nape@coulson.chem.elte.hu, bilqaat@caesar.elte.hu

A theoretical study of the first-order resonance Raman optical activity (ROA) of a single-walled carbon nanotube (SWCNT) is presented for the first time. Tight-binding (TB) Raman and ROA scattering tensors are combined with precise first principles harmonic vibrational modes to obtain scattering intensities. This computational protocol for Raman and ROA spectra has been tested previously for chiral fullerenes, such as C_{76} (J. Chem. Phys., **140**, 044112, 2014). In the present study, this methodology is validated against density functional theory for the alternative case of C_{84}. TB spectral shapes are found to be reliable to determine the absolute configuration of these cage like carbon structures with relatively small curvature. Utilizing the same method, ROA intensities of the (6,5) SWCNT are calculated for three vibrational modes, RBM, G^- and G^+. This tube exhibits approximately five orders of magnitude stronger ROA intensity compared to typical chiral molecules.

Copyright line will be provided by the publisher

1 Introduction As the complete control of the absolute configuration of chiral fullerenes and single-walled carbon nanotubes (SWCNT) becomes increasingly important in applications, more attention turns towards the separation and characterization of these chiral carbon nanostructures (CCNS) (1; 2). CCNS are inherently chiral, which results from the lack of mirror symmetry in their structure. The two non-identical mirror image structures, called an enantiomeric pair, are often present in equivalent quantities, due to achiral synthesis conditions. Enrichment in a single enantiomer of both fullerenes and carbon nanotubes has been achieved only recently (3; 4; 5). Chiral systems exhibit optical activity, i.e. interact differently with left and right circularly polarized light, which is exploited in many variants of chiroptical spectroscopy (6). So far electronic circular dichroism (ECD) (6) was the only tool applied for experimental and theoretical investigations of chiral fullerenes (1; 7; 8) and SWCNT (9; 10; 11).

In this study, we investigate vibrational Raman optical activity (ROA) of CCNS, when optical activity is accompanied by inelastic light scattering and vibrational transition (12). ROA is an excellent complementary method to ECD, since sampling molecular vibrations often reveals much more structural information when studying molecular systems (6; 12; 13). Additionally, all well established Raman techniques for SWCNT characterization (14) may be transferable to ROA.

CCNS ROA measurements have not been reported yet and only a single theoretical ROA study of chiral fullerenes has been published by some of us (15). ROA spectra can not be assigned without computational aid justifying our present focus on the simulation part. Two main factors make ROA computation challenging (16). Firstly, ROA intensities and peak signs are extremely sensitive to the accuracy of calculated molecular structure and harmonic vibrational modes. Secondly, ROA tensors determining scattering intensities are in fact third order properties and have to be evaluated for each individual normal mode.

According to numerical experience (16; 17; 18), time-dependent density functional theory (TD-DFT) provides sufficiently good description of the electronic structure for ROA computations. Although, the recent progress in com-

Copyright line will be provided by the publisher

putational ROA is remarkable (19; 20; 21), CCNS systems accommodating hundreds of carbon atoms are out of the reach of these efficient DFT implementations. Consequently, in our previous study (15), we tested various π-electron models against accurate TD-DFT results on small fullerenes. We have concluded, that for fullerenes ab initio quality ROA spectra can be obtained, if the electron–photon and electron–vibron interactions described by a π-electron model are combined with precise DFT geometry and vibrational modes. If the fullerene curvature, i.e. the rehybridization effect is small enough, even a nearest-neighbour tight-binding (TB) π-electron model reproduces the shape of the ab initio ROA and experimental Raman spectra. The TB absolute intensities are found to be accurate within two orders of magnitude. Strong rehybridization can also be taken into account using a generalized π-electron model, which incorporates interactions between all sites (15).

In this paper, we present further validation of the TB model of Ref. (15) against TD-DFT Raman and ROA spectra for a fullerene with relatively low curvature, namely C_{84}. Experimental Raman intensities and a SWCNT Raman resonance profile is also reproduced with good agreement. Using this validated TB model, the first SWCNT resonance ROA intensities are presented for the (6,5) tube.

2 Theoretical background

2.1 Model Hamiltonian and multipole integrals

A nearest-neighbour one-electron tight-binding model is adopted throughout the present study. Assuming symmetry adapted, orthogonal atomic orbitals ($\chi_\mu(k)$) the field-independent Hamiltonian is given as:

$$\hat{H} = \int \mathrm{d}k \sum_{\mu\,\nu} h_{\mu\nu}(k) \sum_{\sigma} \chi^{+}_{\mu\sigma}(k)\, \chi^{-}_{\nu\sigma}(k)\,, \qquad (1)$$

where $\chi^{+}_{\mu\sigma}(k)$ ($\chi^{-}_{\nu\sigma}(k)$) refers to creation (annihilation) operators of $\chi_\mu(k)$ orbitals with spin σ:

$$\chi_\mu(k) = \sqrt{\frac{a}{2\pi}} \lim_{N\to\infty} \frac{1}{\sqrt{2N+1}} \sum_{n=-N}^{N} \mathrm{e}^{inka} \hat{T}_{na} \chi_\mu\,. \qquad (2)$$

Functions χ_μ are orthogonal atomic orbitals of the reference unit cell. We consider a one-dimensional system lying parallel to the z axis and a denotes the lattice constant in that direction. Operator $\hat{T}_{na}$ translates χ_μ function with $n \cdot a$ in the z direction. The present model considers only one π-electron per atom and the TB hopping integrals, $h_{\mu\nu}$ are only nonzero if atoms μ and ν are nearest neighbours:

$$h_{\mu\nu} \;=\; -h_0\, e^{-\zeta R_{\mu\nu}}\,. \qquad (3)$$

$R_{\mu\nu}$ is the bond length between atoms μ and ν and parameters $h_0 = 243.50486$ eV and $\zeta = 0.3074518$ Å^{-1} are fitted to experimental excitation energies of ethylene and poly-acetylene (22; 23). Since all atoms are identical, diagonal elements of the Hamiltonian are chosen to be zero. The TB lattice sum takes the simple form in Eq. (1):

$$h_{\mu\nu}(k) \;=\; \frac{a}{2\pi}\left(e^{-ika} h_{\mu,\nu^{-1}} + h_{\mu\nu} + e^{ika} h_{\mu,\nu^{+1}}\right),$$

where indices ν^{-1} and ν^{+1} refer to atom ν in the unit cell that precedes and follows the cell of atom μ. The TB model for finite systems can be considered as the $k = 0$ and $N = 0$ special case of the above.

Electron–photon interaction in ROA scattering is described by multipole moments coupled to corresponding components of the electromagnetic field, namely electric and magnetic dipole and electric quadrupole moments. We apply the zero differential overlap (ZDO) approximation to compute multipole moment integrals on the basis of Eq. (2). The approximations in the ZDO multipole integrals and in the nearest-neighbour TB Hamiltonian matrix elements of Eq. (3) are in accord. Explicit formulae of ZDO multipole integrals can be found in Ref. (15) for finite system. Matrix elements of the translational symmetry conserving parts (24) of these multipole operators are analogous. The detailed derivation is going to be shown in a subsequent paper (25).

2.2 Spectral intensities

First order Raman and ROA intensities are determined by polarizability tensors and electromagnetic wave polarization vectors of the incident and scattered light. In the Placzek approximation (6) of these tensors light-matter interaction is treated semi-classically. Additionally, only the lowest order electron–photon coupling terms are taken into account (i.e. dipole approximation in case of the Raman-tensor) and the vibration of the nuclei are described by a harmonic oscillator wavefunction. Using time-dependent perturbation theory and the short-time approximation to describe resonances (19), all three first order Raman and ROA tensors read as

$$\tau_{\alpha\beta}[d^\alpha, V^\beta] = \qquad (4)$$
$$2\int \sum_{j}^{\mathrm{occ}} \sum_{a}^{\mathrm{virt}} \left(\frac{d^\alpha_{ja}(k)\, V^\beta_{aj}(k)}{\omega_{aj}(k) - \omega - i\Gamma} + \frac{V^\beta_{ja}(k)\, d^\alpha_{aj}(k)}{\omega_{aj}(k) + \omega + i\Gamma} \right) \mathrm{d}k\,,$$

where multipole moments, V^β are defined below. Indices j, a refer to occupied and virtual molecular orbitals, ω denotes the energy of the incident light ($\hbar = 1$) and $\omega_{aj}(k) = \varepsilon_a(k) - \varepsilon_j(k)$ quantities are orbital energy differences for a given k value. Greek indices $\alpha, \beta, \gamma, ..$ denote Cartesian components.

Damping parameter of eq. (4), Γ is in reciprocal relation to the lifetime of the virtual excited state of the scattering process (19). Let us note here, that if only one or a few excited states are in resonance, an alternative approach can be applied taking into account vibronic transitions (26; 27). However, in π-electronic structures of large CCNS, many vibronic state could be in resonance, which hinders the explicit treatment of vibronic transitions.

The electric dipole-electric dipole, i.e. Raman tensor determines the dipole moment induced by the electric field:

Copyright line will be provided by the publisher

$\alpha_{\alpha\beta} = \tau_{\alpha\beta}[d^{\alpha}, d^{\beta}]$. Similarly, the electric dipole-magnetic dipole tensor is $G'_{\alpha\beta} = \mathrm{Im}\left(\tau_{\alpha\beta}[d^{\alpha}, m^{\beta}]\right)$ and the electric dipole-electric quadrupole tensor is given as $A_{\alpha,\beta\gamma} = \tau_{\alpha\beta}[d^{\alpha}, \theta^{\beta\gamma}]$ (6). Polarizability tensors for finite systems can be derived from the above taking the limit of $k = 0$. In Placzek's approximation only first derivatives of the above transition polarizabilities contribute to the scattering intensities, according to the Herzberg-Teller expansion (6):

$$\tau^{p}_{\alpha\beta} = \left(\frac{\partial \tau_{\alpha\beta}}{\partial Q_p}\right)_0$$

Numerical differentiation with respect to normal coordinates, Q_p are carried out using a step size of 10^{-3} bohr. Note that derivatives $\tau^{p}_{\alpha\beta}$ incorporate both electron–phonon and photon–phonon coupling.

Typically, ROA is measured in solution phase, in which case tensor derivatives have to be averaged over all possible spatial orientations. The resulting spectroscopic invariants necessary in our case are as follow:

$$\beta_{\mathrm{S}}(\alpha)^2,\ \beta_{\mathrm{A}}(\alpha)^2,\ \beta_{\mathrm{S}}(G')^2,\ \beta_{\mathrm{S}}(A)^2 \text{ and } \beta_{\mathrm{A}}(A)^2,$$

using conventional notations (12; 19). Raman and ROA scattering cross sections are evaluated for the experimentally available backscattering arrangement with unpolarized incident light (12):

$$\mathrm{d}\sigma_u^{\mathrm{Raman}} = K\left[90\,\mathrm{Tr}(\alpha^2) + 14\,\beta_{\mathrm{S}}(\alpha)^2 + 10\beta_{\mathrm{A}}(\alpha)^2\right], \quad (5)$$

$$\Delta\mathrm{d}\sigma_u^{\mathrm{ROA}} = \frac{4K}{c}\left[12\,\beta_{\mathrm{S}}(G')^2 + 4\,\beta_{\mathrm{S}}(A)^2 + 2\,\beta_{\mathrm{A}}(A)^2\right], (6)$$

where $K = (1/90)\,(\mu_0/(4\pi))^2\,(\omega - \omega_p)^3\,\omega$ and μ_0 is the permeability of vacuum, c is the speed of light and ω_p is the harmonic frequency associated to normal mode Q_p. Raman and ROA intensities have the same form as the cross sections in Eqs. (5) and (6), with $K = 1$ prefactor.

2.3 Dynamical matrix and normal modes

Normal modes of fullerenes are obtained by the traditional GF method. To reduce the computational cost of the normal modes of carbon nanotubes in their translational unit cell, helical symmetry can be exploited. The translational unit cell of a nanotube can be built from two carbon atoms in its helical unit cell using rotations and screw axis symmetry operations (28). Analogously, it is sufficient to compute force constant matrix elements between these two atoms in the reference helical cell and their images to construct the dynamical matrix in the translational unit cell. The resulting $N_{\mathrm{h}} 6 \times 6$ Hessian elements are transformed by the above symmetry operations to obtain the missing elements of the dynamical matrix (28; 29; 30). (N_{h} is the number of helical symmetry equivalent atom pairs in the translational unit cell.) Finally, normal modes in the translational picture are obtained by diagonalization.

3 Results and discussion

Raman and ROA scattering cross sections are computed for a chiral fullerene and a chiral SWCNT.

3.1 Computational details

One of the most common and intensively studied chiral fullerene (1; 5; 31), C_{84} has been chosen to assess the TB approximation against TD-DFT ROA spectrum. There are 24 isolated pentagon rule obeying isomers of C_{84}, from which the common and stable isomer with D_2 point group symmetry is number 22, using standard nomenclature (1). All spectra are reported for the ^{f}C-D_2-C_{84}(22) configuration (32). In the following we refer to this structure shortly as C_{84}.

In the absence of experimental ROA measurements for CCNS, accurate ab initio computations can serve as benchmark for TB results. Exploiting full spatial symmetry of D_2-C_{84} the TD-DFT ROA spectrum is computed with B3LYP density functional and rDSP basis set (33). For fullerenes, rDSP is identical to 3-21+G and it is a computationally affordable basis set, that can provide ROA spectra in good agreement with experiment for molecular systems (20; 34). TB polarizability tensor derivatives are computed by a local implementation.

C_{84} equilibrium structure and normal modes are obtained at the B3LYP/6-31G* level of theory with the Gaussian 09 program package (35). The necessary components of the dynamical matrix of (6,5) have been calculated using the VASP program (36) with 400 eV plane wave energy cutoff. Additional details can be found in Ref. (37). For SWCNT (6,5), the three Raman active modes of interest are the radial breathing mode (RBM) and the two tangential modes, G^- and G^+. Vibrational frequencies as computed by the above method are 315.8 cm^{-1} , 1549.6 cm^{-1} and 1594.7 cm^{-1} , respectively.

Following the protocol established in Ref. (15), the ab initio molecular structure and vibrational modes underlying the TD-DFT and TB tensor derivatives are the same. Thus, only the quality of the Raman and ROA tensor derivatives wrt. Cartesian coordinates is tested, when TD-DFT and TB spectra are compared.

Raman and ROA cross sections for a given vibrational frequency are depicted as Lorentzian curves with 5 cm^{-1} linewidth. The spectral region of C_{84} in Figs. 1 and 2 are split into two intervals: [200 cm^{-1} , 1000 cm^{-1}] and [1000 cm^{-1} , 1800 cm^{-1}]. Separate presentation of these two ranges allows better perceptibility of the less intense peaks in the smaller wavenumber region. To assist visual comparison further, areas below spectral curves are normalized separately for the split intervals. Relative normalization factors (RNFs) shown in figure labels as ”xRNF” are ratios of the reference TD-DFT and the analyzed TB areas under spectral curve. RNFs are indicators of the agreement in relative intensity, while peak structures can be compared best on the normalized spectra.

SWCNT scattering cross sections are evaluated at incident light frequencies close to resonance. Although damping parameter Γ is generally system dependent, $\Gamma = 0.109\,\mathrm{eV}$ has been applied in all presented computations (19). Numerical integration for polarizabilities in the translational Brillouin zone has converged using 41 equidistantly placed points.

3.2 C_{84} fullerene Raman spectra of C_{84} are plotted in Fig. 1 at 1064 nm incident light. The experimental spectrum available for a smaller wavenumber region ([200 cm^{-1} , 500 cm^{-1}]) (38) compares well with the B3LYP/rDSP spectrum. We therefore conclude that, the quality of the TB spectrum can be evaluated against the B3LYP/rDSP. Inspecting Fig. 1, one can find good agreement in the relative peak intensities of the TB and B3LYP methods, especially in the higher wavenumber region. The TB absolute intensities are overestimated by two orders of magnitude compared to DFT. As pointed out in Ref. (15), this behavior is typical for the TB method and originates mainly in the underestimated HOMO-LUMO gap, which appears in the denominator of Eq. (4).

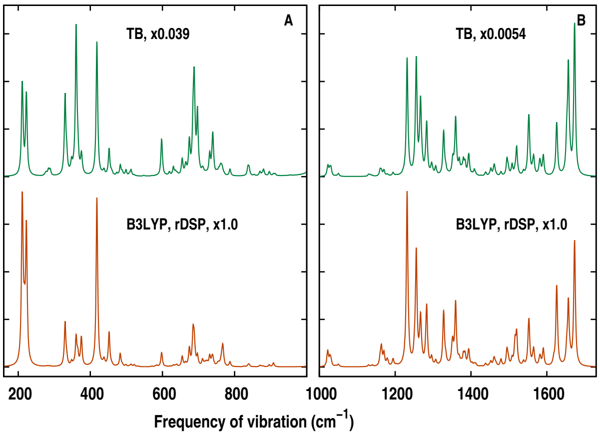

Figure 1 Unpolarized backscattering Raman cross sections of C_{84} at 1064 nm. See text for further notations.

Additionally, there is factor of 7.2 difference in the RNF values of the lower and higher wavenumber ranges. This can be interpreted considering the qualitative difference in the nature of normal coordinates in these two intervals. Analogously to the well-known case of C_{60} (39), vibrations of C_{84} (and C_{76}) with smaller frequencies show stronger radial character, while higher-frequency normal modes are basically tangential and contain more stretching component. Inspecting Eq. (3), it is evident, that a TB model parametrized based on bond lengths can describe stretching modes better and approximates electron–vibron coupling for modes with higher bond angle and torsion component worse. Accordingly, a generalized π-electron model, which incorporates curvature effects, performs more consistently in this respect (15).

In case of ROA, due to the lack of experimental data, comparison can only be made between TB and TD-DFT results. ROA spectra in Fig. 2. show slightly less, but still good agreement with TD-DFT. Only three major deviations can be found, namely in peak structures around 330-360 cm^{-1} , 1550-1590 cm^{-1} and 1640-1680 cm^{-1} (see highlighted areas in Fig. 2.). TB absolute ROA intensities are overestimated by three orders of magnitude, and RNF values in panels A and B differ by a factor of 5.8. Obviously, errors from the curvature effects and the underestimated gap appear in both Raman and ROA tensors.

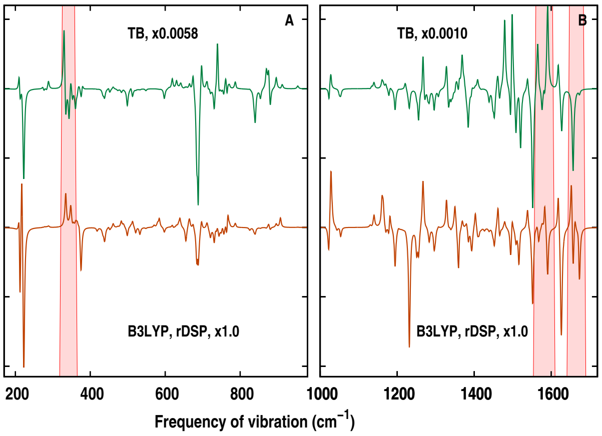

Figure 2 Unpolarized backscattering ROA cross sections of C_{84} at 1064 nm. See text for further notations.

In Ref. (15) an extensive investigation has been conducted for D_2-C_{76} and D_2-C_{28}. The numerical performance of the same TB model against TD-DFT in case of D_2-C_{76} is also good, in agreement with the present results for D_2-C_{84}. However, for fullerenes with larger curvature, such as D_2-C_{28}, TB is incapable to describe scattering cross sections and should not be used.

Since the ROA spectra of two enantiomers are identical in absolute value and opposite in sign, the identification of absolute configurations is based on the intensive peaks with matching signs and similar intensity. The majority of ROA peaks are well-described by the TB model, thus it can be considered a useful aid to distinguish enantiomers of CCNS similar to higher fullerenes, such as C_{84} and C_{76}.

3.3 Carbon nanotube The case of nanotubes differs from the fullerenes in two aspects. First of all, only three intense peaks appear in SWCNT first-order Raman spectrum. Secondly, SWCNT have smaller band gaps, therefore, the 1064 nm incident light is already close to resonance with their first electronic transition. In the present study the (6,5) tube is introduced as an illustrative example. Detailed comparison of the ROA spectra of further nanotubes will be the subject of a subsequent publication (25).

Relative Raman and ROA intensities are listed in Tables 1 and 2 for several incident light frequencies. The most intense lines of a small organic molecule, methyloxirane (C_3H_4O) is chosen as reference. Our intention is to investigate trends and provide information on the intensities of SWCNT ROA peaks compared to routinely measured chiral molecules. Comparison of relative intensities is beneficial, as they show smaller dependence on the vibrational frequency of an actual normal mode and on experimental circumstances. Raman and ROA spectra of methyloxirane is computed using B3LYP density functional and aug-cc-pVDZ basis set at 1064 nm (20; 35). The reference line intensities of C_3H_4O are 335.2 $\mathrm{\AA}^4$/amu and 0.0329 $\mathrm{\AA}^4$/amu for Raman and ROA, respectively.

First, we discuss the Raman intensities in Table 1. A significant increase of the intensity can be observed as the frequency of the laser light is approaching 1064 nm from both directions, which indicates a resonance behavior.

Table 1 Relative resonance Raman intensities of the SWCNT (6,5) for various incident light frequencies.

Laser freq. [nm]	RBM	G^-	G^+
532	$7.98\cdot10^6$	$1.34\cdot10^8$	$5.13\cdot10^8$
1064	$2.91\cdot10^7$	$6.93\cdot10^8$	$2.33\cdot10^{10}$
1596	$3.98\cdot10^6$	$1.41\cdot10^8$	$6.45\cdot10^8$
2128	$2.80\cdot10^6$	$1.07\cdot10^8$	$2.93\cdot10^8$

To investigate this tendency further let us look at the calculated resonance Raman profile of SWCNT (6,5) in Fig. 3. The RBM intensity is scaled by a factor of 1000, while G^- is multiplied by 50 to match the magnitude of G^+. The region of strong resonance indicates that the first electronic excitation energy is around 1.2 eV, in good agreement with the experimental value of 1.26 eV (40). Turning back to Table 1, it is obvious that 1064 nm = 1.17 eV is the closest to resonance. Higher wavelengths go away from the resonance, while the case of 532 nm = 2.33 eV is close to the second optical transition at 2.17 eV (40).

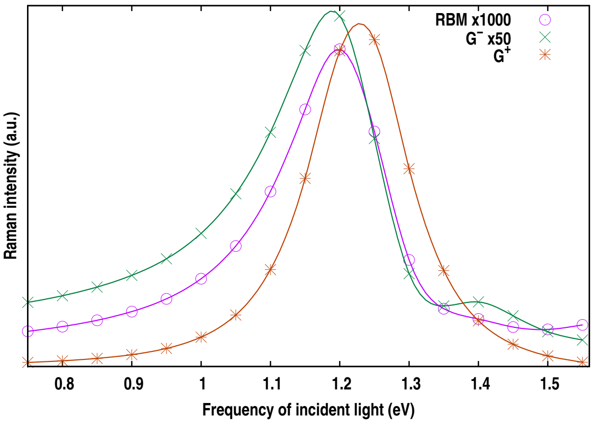

Figure 3 Resonance Raman profile of SWCNT (6,5) using TB approximation.

Looking at Fig. 3 and Table 1, there is a significant difference in the relative intensities of the three Raman active modes of (6,5). Since C_{84} and (6,5) have comparable diameters, cca. 8.0 Å and 7.5 Å, curvature effects are expected to be similar. The RBM mode is subjected to the biggest effect, due to its radial nature, while the G^- and G^+ are tangential and mostly stretching modes. However, G^+ is almost parallel to the tube axis, while G^- is practically perpendicular to it. That is why the G^- intensity is more affected by the curvature and deviates from the intensity of G^+. Therefore we take into account the unbalanced quality of TB intensities and consider G^+ intensities the most reliable. Based on the comparison against TD-DFT on fullerenes, TB SWCNT ROA intensities are expected to be accurate within a few orders of magnitude and we only draw conclusions accordingly.

Similar resonance behavior is found in case of ROA (Table 2). Additionally, the signs, important to determine the absolute configuration, are flipping. It is apparent from Tables 1, 2 and Fig. 3, that Raman and consequently ROA spectra depend strongly on the laser frequency. There might exist a relation between the structure of SWCNT, the laser frequency and the ROA signal sign, but the present data are yet insufficient to study such trends in numerical terms. Therefore, one has to rely on computational aid to successfully assign experimental ROA SWCNT spectra.

Table 2 Relative resonance ROA intensities of the SWCNT (6,5) for various incident light frequencies.

Laser freq. [nm]	RBM	G^-	G^+
532	$-1.52\cdot10^5$	$-6.93\cdot10^6$	$5.67\cdot10^4$
1064	$1.13\cdot10^5$	$5.16\cdot10^6$	$9.68\cdot10^7$
1596	$-1.40\cdot10^4$	$-9.08\cdot10^5$	$4.84\cdot10^6$
2128	$-9.43\cdot10^3$	$-5.67\cdot10^5$	$3.19\cdot10^6$

Finally, we raise the question whether ROA of SWCNT could in effect be measurable despite experimental difficulties, such as small sample quantity and small enantiomeric excess. Looking at Table 2, the relative ROA intensity is almost 10^8 with the TB model for G^+ near resonance. Counting with the factor of 1000 overestimation in TB intensity this TB result could be translated into a roughly five order of magnitude difference between ROA intensity of SWCNT and measurable small organic molecules. For comparison, the same intensity ratio in case of C_{84} and C_{76} are around 16 and 1200. This incredibly strong signal can be attributed to two effects, to the close to resonance laser frequency and to the uniquely long helical structure of SWCNT and could be amplified even more with a laser frequency tuned to an electronic transition.

4 Conclusion Theoretical Raman and ROA spectra of chiral fullerenes and a chiral carbon nanotube have been obtained based on the combination of TB scattering tensors and DFT vibrational modes. This methodology is found to be computationally efficient and reliable for CCNS according to comparison with TD-DFT scattering cross sections. The sign pattern of computed ROA intensities could provide the necessary aid to determine CCNS absolute configurations. Intensive CCNS ROA signals being up to five orders of magnitude stronger than the intensities of frequently measured chiral molecules may motivate forthcoming experiments.

Besides TB and DFT ROA spectra of C_{84}, first-order resonance ROA intensities of the (6,5) nanotube is evaluated for the first time. Intensities as a function of incident laser frequency show a resonance profile, similar to the well-known case of the Raman spectra of SWCNT. Therefore tuning the laser frequency to an electronic transition, absolute configuration of a single nanotube might be determined with ROA microscopy.

Acknowledgements This work has been supported by the Hungarian National Research Fund (OTKA), grant numbers K-81588 and K-81492 and the supercomputing facility of the National Information Infrastructure Development Institute (NIIF).

References

[1] F. Hidalgo and C. Noguez, Physica Status Solidi (B) **247**, 1889–1897 (2010).
[2] X. Q. Chen, X. Y. Liao, J. G. Yu, F. P. Jiao, and X. Y. Jiang, Nano **08**, 1330002 (2013).
[3] X. Peng, N. Komatsu, S. Bhattacharya, T. Shimawaki, S. Aonuma, T. Kimura, and A. Osuka, Nature Nanotechnology **2**, 361–5 (2007).
[4] X. Peng, F. Wang, A. K. Bauri, A. F. M. M. Rahman, and N. Komatsu, Chemistry Letters **39**, 1022–1027 (2010).
[5] E. M. Pérez and N. Martín, Organic & Biomolecular Chemistry **10**, 3577–83 (2012).
[6] L. D. Barron, Molecular Light Scattering and Optical Activity (Cambridge University Press, 2004).
[7] J. Crassous, J. Rivera, N. S. Fender, L. Shu, L. Echegoyen, C. Thilgen, A. Herrmann, and F. Diederich, Angewandte Chemie International Edition **38**, 1613–1617 (1999).
[8] F. Furche and R. Ahlrichs, Journal of the American Chemical Society **124**, 3804–5 (2002).
[9] A. Green, M. Duch, and M. Hersam, Nano Research **2**, 69–77 (2009).
[10] A. Sánchez-Castillo and C. Noguez, J. Phys. Chem. C **114**, 9640–9644 (2010).
[11] G. Liu, F. Wang, S. Chaunchaiyakul, Y. Saito, A. K. Bauri, T. Kimura, Y. Kuwahara, and N. Komatsu, Journal of the American Chemical Society **135**, 4805–14 (2013).
[12] L. A. Nafie, Vibrational Optical Activity: Principles and Applications (John Wiley & Sons, 2011).
[13] L.D. Barron and A.D. Buckingham, Chemical Physics Letters **492**, 199–213 (2010).
[14] M. Dresselhaus, A. Jorio, and R. Saito, Annu. Rev. Cond. Mat. Phys. **1**, 89–108 (2010).
[15] P. R. Nagy, P. R. Surján, and Á. Szabados, The Journal of Chemical Physics **140** (2014).
[16] K. Ruud and A. J. Thorvaldsen, Chirality **21**, 54–67 (2009).
[17] M. Pecul and K. Ruud, International Journal of Quantum Chemistry **104**, 816–829 (2005).
[18] T. D. Crawford, Theoretical Chemistry Accounts **115**, 227–245 (2005).
[19] L. Jensen, J. Autschbach, M. Krykunov, and G. C. Schatz, The Journal of Chemical Physics **127**, 134101 (2007).
[20] J. R. Cheeseman and M. J. Frisch, Journal of Chemical Theory and Computation **7**, 3323–3334 (2011).
[21] A. J. Thorvaldsen, B. I. N. Gao, K. Ruud, M. Fedorovsky, G. Zuber, and W. Hug, Chirality **24**, 1018–1030 (2012).
[22] J. Kürti and P. R. Surján, J. Math. Chem. **10**, 313–327 (1992).
[23] P. R. Surján, A. Lázár, and M. Kállay, Phys. Rev. B **58**, 3490 (1998).
[24] P. Otto, Phys. Rev. B **45**, 10876–10885 (1992).
[25] P. R. Nagy, L. Biró, J. Koltai, P. R. Surján, Á. Szabados, and J. Kürti, In preparation.
[26] L. Nafie, Theoretical Chemistry Accounts **119**, 39–55 (2008).
[27] S. Luber, J. Neugebauer, and M. Reiher, The Journal of Chemical Physics **132**, 044113 (2010).
[28] Á. Rusznyák, J. Koltai, V. Zólyomi, and J. Kürti, Physica Status Solidi (b) **246**, 2614–2617 (2009).
[29] C. X. Cui and M. Kertesz, The Journal of Chemical Physics **93**, 5257–5266 (1990).
[30] V. Zólyomi, J. Koltai, J. Kürti, and H. Kuzmany, in: DFT calculations on fullerenes and carbon nanotubes, edited by V. Basiuk and S. Irle, (Signpost Publisher, Kerala, India, 2008).
[31] T. Jovanovic, D. Koruga, and B. Jovancicevic, Diamond and Related Materials **44**, 44 – 48 (2014).
[32] C. Thilgen and F. Diederich, Chemical Reviews **106**, 5049–135 (2006).
[33] G. Zuber and W. Hug, The Journal of Physical Chemistry A **108**, 2108–2118 (2004).
[34] M. Reiher, V. Liégeois, and K. Ruud, The Journal of Physical Chemistry A **109**, 7567–74 (2005).
[35] M. J. Frisch, G. W. Trucks, H. B. Schlegel, G. E. Scuseria, M. A. Robb, J. R. Cheeseman, and et al., Gaussian 09 Revision C.1, Gaussian Inc. Wallingford CT 2009.
[36] G. Kresse and J. Hafner, Phys. Rev. B **47**, 558–561 (1993).
[37] J. Koltai, V. Zólyomi, and J. Kürti, Physica Status Solidi (b) **245**, 2137–2140 (2008).
[38] M. Krause, M. Hulman, H. Kuzmany, T. J. S. Dennis, M. Inakuma, and H. Shinohara, AIP Conference Proceedings **486**, 136–139 (1999).
[39] S. Dresselhaus, G. Dresselhaus, and P. Eklund, Science of Fullerenes and Carbon Nanotubes (Academic Press, 1996).
[40] L. Kavan, O. Frank, A. A. Green, M. C. Hersam, J. Koltai, V. Zólyomi, J. Kürti, and L. Dunsch, The Journal of Physical Chemistry C **112**, 14179–14187 (2008).

Copyright line will be provided by the publisher